Applied Surface Science 487 (2019) 918–929

Contents lists available at ScienceDirect

Applied Surface Science

journal homepage: www.elsevier.com/locate/apsusc

Full length article

XPS and Kelvin probe studies of SnO_2/RGO nanohybrids based NO_2 sensors

Bhagyashri Bhangare[a,b], Niranjan S. Ramgir[b,*], Shweta Jagtap[c], A.K. Debnath[b], K.P. Muthe[b], Chiaki Terashima[d], Dinesh K. Aswal[b,e], Suresh W. Gosavi[a,*], Akira Fujishima[d]

[a] Center for Advanced Studies in Material Science and Solid-State Physics, Department of Physics, Savitribai Phule Pune University, Pune 411 007, India
[b] Technical Physics Division, Bhabha Atomic Research Centre, Mumbai 400 085, India
[c] Department of Instrumentation Science, Savitribai Phule Pune University, Pune 411 007, India
[d] Photocatalysis International Research Centre, Tokyo University of Science, Chiba 278-8510, Japan
[e] CSIR-National Physical Laboratory, Dr. K. S. Krishnan Marg, New Delhi 110 012, India

ARTICLE INFO

Keywords:
SnO_2/RGO
Nanohybrids
Chemiresistive sensors
Elovich model
NO_2 sensor

ABSTRACT

The present paper reports the successful detection of NO_2 using the hydrothermally synthesized SnO_2/RGO nanohybrids. The nanohybrids successfully detected NO_2 below its threshold limit value (TLV) with a minimum detection limit of 0.5 ppm. The 3-fold sensor response (R_g/R_a) was obtained towards 3 ppm of NO_2 at an operating temperature of 200 °C. Importantly, the nanohybrids exhibited faster response kinetics. For example, the response and the recovery times of 10 and 40 s, respectively were obtained for 1 ppm NO_2 exposure. In nanohybrids, the particle size of SnO_2 is ~5–7 nm which is comparable to twice of its Debye length (3 nm) and accordingly, benefits the charge transport and the sensor response. NO_2 adsorption on the sensor surface is further studied using the Elovich model. The obtained results were further corroborated with the observations from X-ray photoelectron spectroscopy (XPS) and Kelvin probe studies performed before and after exposure to NO_2. The considerable long-term stability and selectivity indicate that the developed sensor can find a promising application in NO_2 detection.

1. Introduction

The development of industrial centres in urban areas effectively concentrates the environmental hazardous gases such as benzene, nitrogen oxide, carbon monoxide, ozone and particular matter ($PM_{2.5}$) [1]. As per the World Health Organization (WHO) around seven million deaths have been reported globally due to adverse air pollution [2]. For the developing countries like India, the pollution at major cities like New Delhi and Mumbai is at an alarming concentration and needs to be addressed urgently. Heavy transportation in these cities is considered to be the major source of air pollution. Of the various pollutants, nitrogen dioxide (NO_2) is a strong oxidizer and has adverse effect on both wild life and human. In particular, it is one of the major pollutants responsible for the ozone layer depletion and acid rains. Further, NO_2 is known to give finger prints for the chronic obstructive pulmonary diseases (COPD) and thereby its trace amount detection in medical fields is highly desired. Its threshold limit value (TLV, indoor) as stated by the Occupational Safety and Health Administration (OSHA) is 5 ppm [3]. Besides, for NO_2 the short-term (STEV, 15 min) and long-term exposure value (LTEV, 8 h) are 5 and 3 ppm, respectively as stated by ACGIH (American Conference of Governmental Industrial Hygienists also known as Association Advancing Occupational and Environmental Health). Accordingly, detection of NO_2 below this concentration is of prime need. Various detection approaches namely optical [4], fluorescence [5], and electrochemical [6] have been attempted for the trace amount NO_2 detection. But most of them are either bulky in nature or often time-consuming. Being lighter in weight and possibility of quicker detection suggests chemiresistive gas sensors to be the best alternative. Besides they offer numerous advantages like real-time detection, ease of operation, miniaturization, and overall cost-effectiveness [7,8].

Several metal oxide semiconductors (MOS) along with the inorganic/organic or inorganic/inorganic nanocomposites like ZnO-RGO (Reduced Graphene Oxide), ZnO-MWCNTs (Multiwalled Carbon Nanotubes) and NiO-CuO have been reported for the chemiresistive gas sensing application [9–11]. Most of the MOS showed good sensor response at higher operating temperatures as it provides more energy to accelerate the charge carriers between the analytes and the sensing material. Incorporation of noble metal as sensitizers has been reported to be an effective way for enhancing the sensing properties of semiconductor gas sensors [12,13].The noble metal doped SnO_2/RGO nanohybrids have also been reported for the detection of VOCs (volatile organic compounds) with improved sensor characteristics as compare

* Corresponding authors.
E-mail addresses: niranjanpr@yahoo.com (N.S. Ramgir), swg@physics.unipune.ac.in (S.W. Gosavi).

https://doi.org/10.1016/j.apsusc.2019.05.176
Received 8 March 2019; Received in revised form 26 April 2019; Accepted 15 May 2019
Available online 17 May 2019
0169-4332/

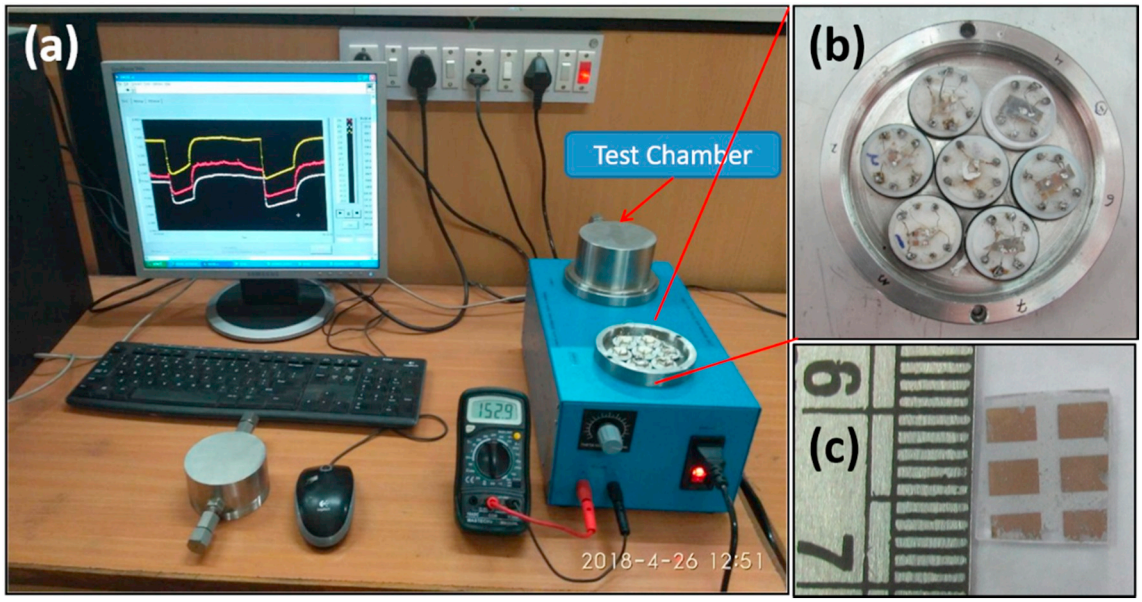

Fig. 1. (a) Table-top static gas sensing unit used for the sensing measurement, (b) magnified image of the test chamber showing the seven-sensor head on which the individual sensors can be mounted, and (c) photograph of the sensors deposited on to the glass substrates with gold electrodes.

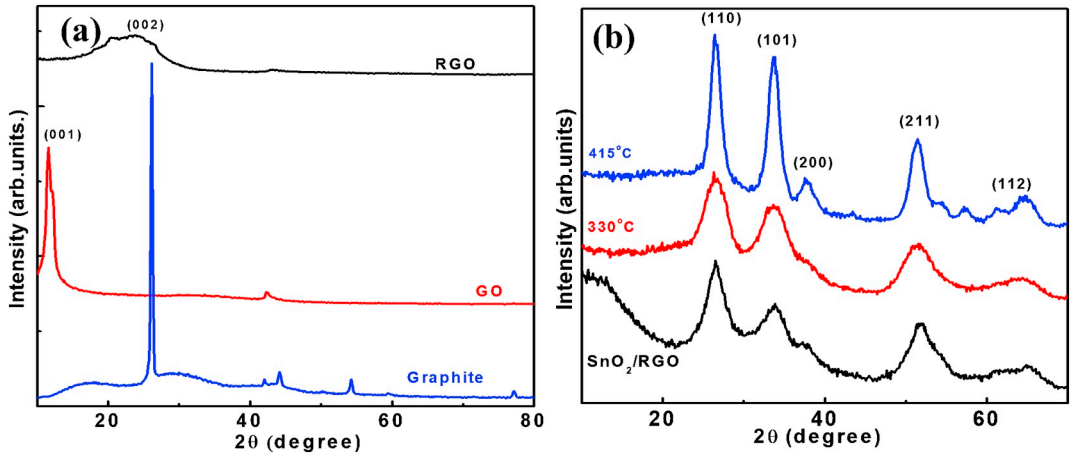

Fig. 2. (a) XRD pattern of graphite, graphite oxide, RGO, and (b) effect of annealing temperature on the XRD pattern of SnO_2/RGO nanohybrids.

to that of the pristine one [14,15].

The sensitivity has a strong dependence on the oxygen adsorption taking place on the sensor surface. The sensing mechanism basically includes the change in electrical resistance as a result of oxidation/reduction processes occurring on the sensor surface due to adsorption/desorption of analytes [16]. Among the reported MOS, SnO_2 an n-type semiconductor having a band gap of 3.6 eV (300K) is widely studied [17]. Its inherent non-stoichiometry and ease of adsorption of oxygen on the surface has resulted in sensors that are highly sensitive towards various analytes. But numerous drawbacks such as low sensitivity, slow response/recovery rate and high-power consumption due to operation at elevated temperatures have restricted its utility. Current research is focused on the sensitivity/selectivity enhancement and lowering of operating temperatures via the use of nanostructures, their functionalization and doping [18,19]. In particular, use of nanohybrids employing functionalized carbon materials such as graphene, carbon nanotubes and nanodiamonds have resulted in an improved response characteristic.

Among these carbon nanomaterials, graphene is the most desirable one, due to its high surface area to volume ratio, high charge carrier mobility (200,000 cm^2/V·s at room temperature), good mechanical strength and the possibility to detect single molecule adsorption/desorption. The presence of oxygen moieties such as epoxides, alcohols, and carboxylic acids gives the chemically derived graphene/RGO different chemical structures. In GO, these different oxygen functional groups result in electrically insulating behaviour. Chemical reduction results in the removal of oxygen functionalities and restoration of aromatic sp^2 hybridized carbons. The chemical reduction method does not yield pure graphene, as some of the oxygen groups still attached to the basal planes and at the edges. Thus, RGO is conducting with chemically active defect sites making it a promising active material for sensor application. Further, its chemical functionalization with metal and metal oxide nanoparticles could readily allow low concentrations detection of numerous analytes. Although various metal oxide/RGO based nanohybrids have been reported, the detailed investigation and correlations between theoretical and experimental approaches in gas sensing mechanism are still needed to be established.

Gas sensing is a surface phenomenon wherein the top 5–10 nm of surface plays a crucial role in the governing sensing mechanism. In semiconductors, the surface chemistry of physisorbed ions (O^{2-} or O^-) affects the band bending model and predicts the dependency of steady-state sensor response and temperature. The surface properties can

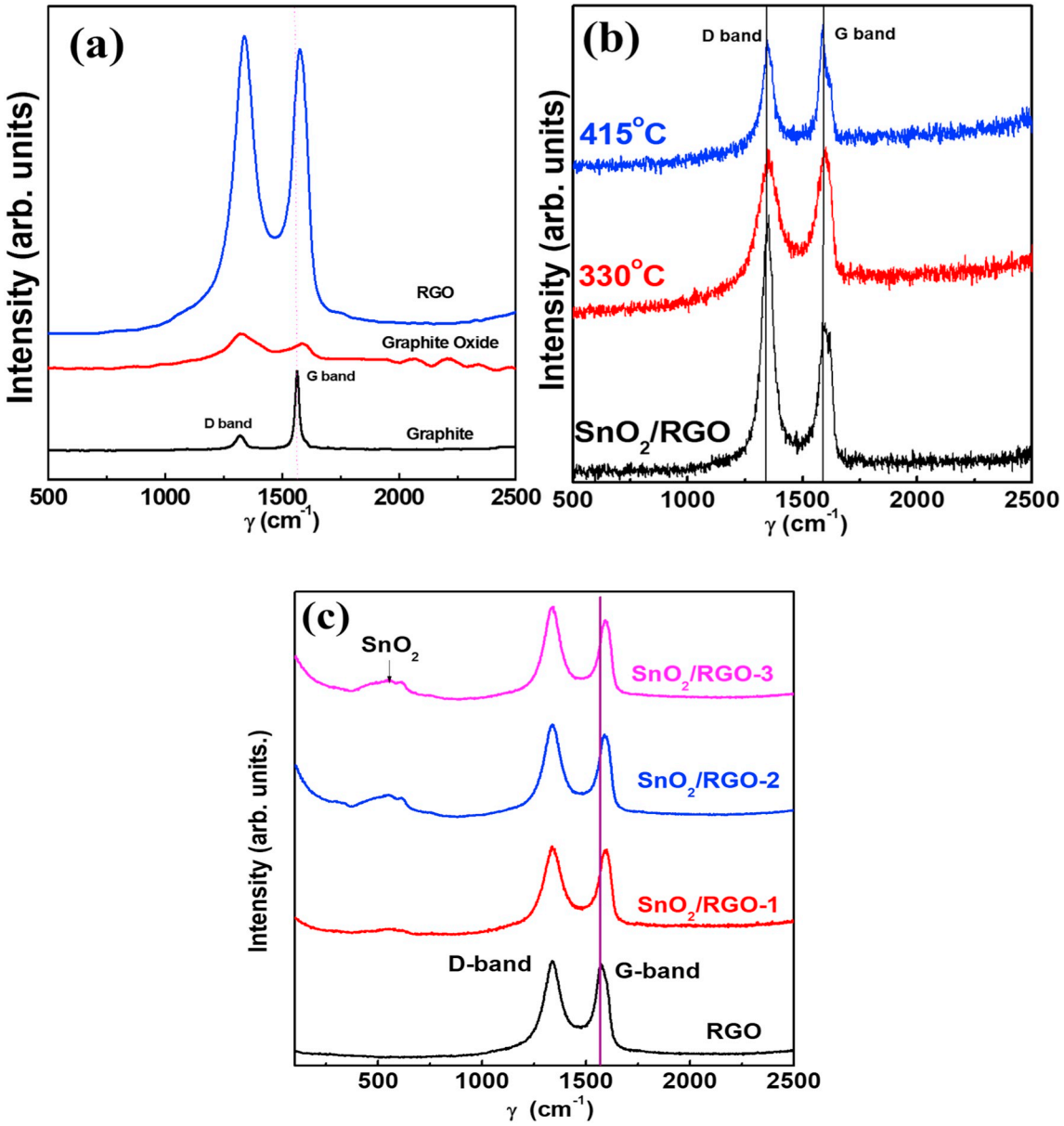

Fig. 3. (a) Raman spectra of graphite, graphite oxide, RGO and (b) comparative Raman spectra of un-annealed and annealed SnO_2/RGO nanohybrids at 330 and 415 °C, respectively, (c) Raman spectra for different Sn/GO ratio in nanohybrids.

Table 1
Relative I_D/I_G ratio of SnO_2/RGO nanohybrids.

Sr. no.	Samples	D-band (cm^{-1})	G-band (cm^{-1})	I_D/I_G	Defect density, n_d (cm^{-2})
1.	Graphite	1326	1560	0.25	1.62 e^{40}
2.	Graphite oxide	1326	1585	1.24	4.00 e^{41}
3.	RGO	1326	1572	0.96	2.40 e^{41}
4.	SnO_2/RGO	1352	1599	1.67	7.26 e^{41}
5.	SnO_2/RGO (330 °C)	1348	1604	0.99	2.55 e^{41}
6.	SnO_2/RGO (415 °C)	1350	1604	0.90	2.11 e^{41}
7.	SnO_2/RGO-1	1342	1603	1.72	7.70 e^{41}
8.	SnO_2/RGO-2	1342	1599	1.88	9.20 e^{41}

further be controlled or monitored by engineering of Fermi level, work function, ionization energy/electron affinity, charge carrier injection and transport. Kelvin probe is one such technique that allows the monitoring of variation in the work function induced in the sensing layer upon gas interaction. This can be further used to determine the surface band bending. In the present work, an NO_2 sensor is realized exploiting the advantages offered by SnO_2 and RGO in a nanohybrid film form. The developed nanohybrid responded reversibly towards NO_2 at 200 °C. Moreover, the NO_2 adsorption kinetics is investigated using the Elovich model, pseudo second order equation and the underlying sensing mechanism is established with the help of results obtained from gas sensing, XPS and Kelvin Probe studies.

2. Experimental section

2.1. Synthesis of graphene oxide and SnO_2/RGO nanohybrids

Graphite oxide was synthesized using a modified Hummer's method. To obtain the graphene oxide (GO), the graphite oxide was dissolved in distilled water (2 mg/ml) and subjected to ultrasonication for 3 h. The obtained GO suspension was then used for the synthesis of SnO_2-RGO nanohybrids via hydrothermal route. For this, polyethylene glycol (1 g) and stannous chloride ($SnCl_4.5H_2O$, 2.1 g) were dissolved in solution mixture (GO/Ethanol, 2:1 vol.) and subjected to hydrothermal growth

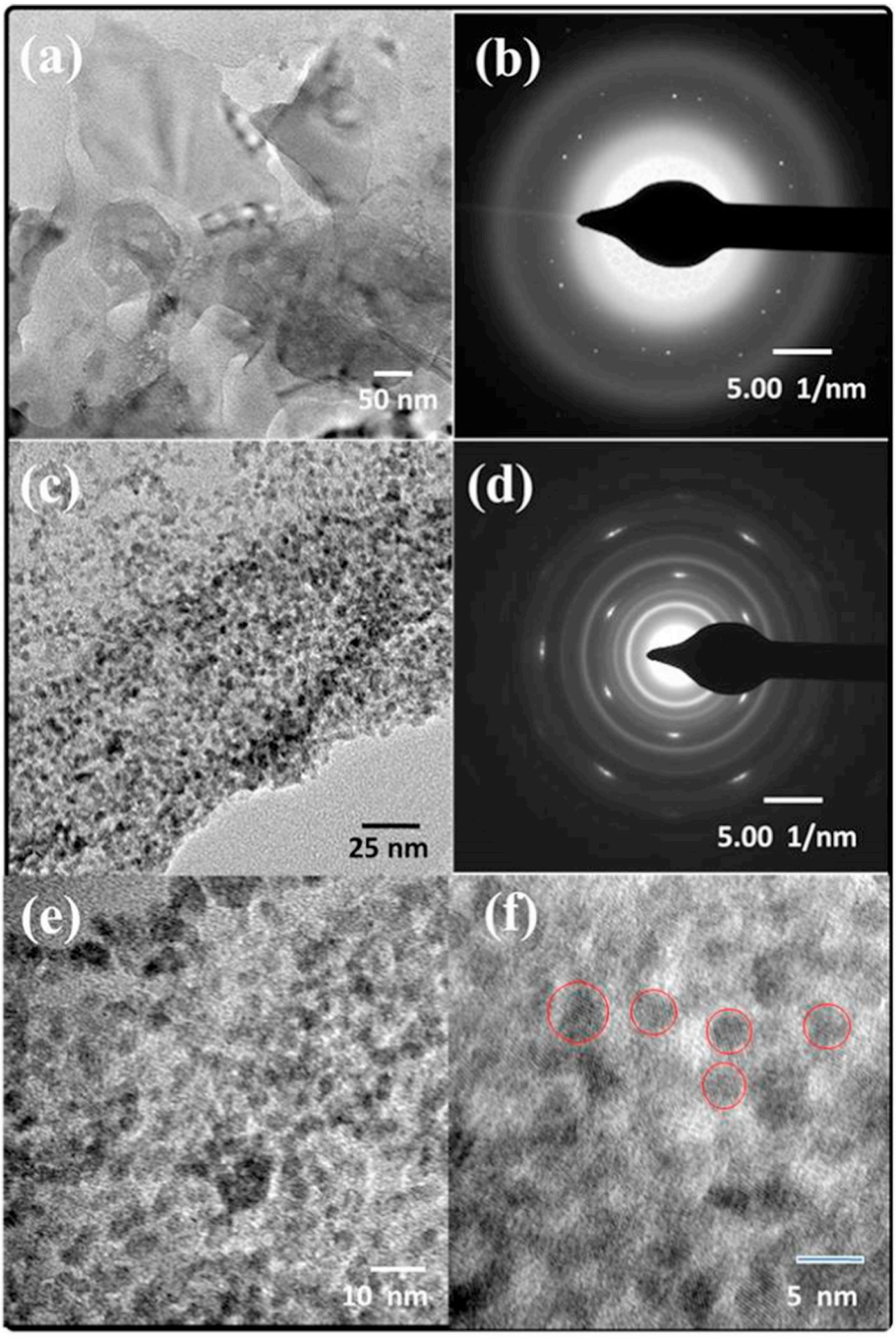

Fig. 4. TEM micrographs of RGO and SnO_2/RGO nanohybrid (a, c), corresponding SAED pattern, (b, d), and (e, f) high-resolution TEM image of SnO_2/RGO nanohybrid.

at 180 °C for 7 h. The reaction mixture was cooled to room temperature, centrifuged in ethanol and dried at 90 °C in an oven so as to obtain the SnO_2-RGO nanohybrids powder. For comparison, pure RGO was also synthesized using a similar method but without the addition of stannous chloride. The SnO_2/RGO nanohybrids were synthesized in different compositions containing Sn/GO in weight ratios of 13.2, 15.6 and 18.7. These were named as SnO_2/RGO, SnO_2/RGO-1, and SnO_2/RGO-2, respectively.

2.2. Structural and morphological characterization

XRD measurements were carried out using Bruker AXS D8 Advance X-ray diffractometer (CuKα, λ = 1.5406 Å). Raman measurements were performed using Renishaw Raman spectrometer (laser source: 514 nm). The morphological analysis was carried out using a transmission electron microscope (TEM) TECNAI G2 20 (operating voltage 80–300 keV). X-ray photoelectron spectroscopy (XPS) measurements were performed using Mg-Kα (1253.6 eV) source (RIBER system) and DESA-150 electron analyzer (Staib Instruments, Germany). The binding energy calibration was carried out using the Au $4f_{7/2}$ peak at 84 eV. Similarly, the effect of NO_2 on Fermi level and work functions were investigated using the SKP Kelvin Probe 4.5 from KP Technology Ltd., UK [20]. The XPS and Kelvin probe measurements were performed ex-situ [21,22]. For this the sensor films were kept at an operating temperature of 200 °C in the gas sensing unit and exposed to 10 ppm of NO_2 for 130 s (response time). After the exposure, the sensor films were removed and

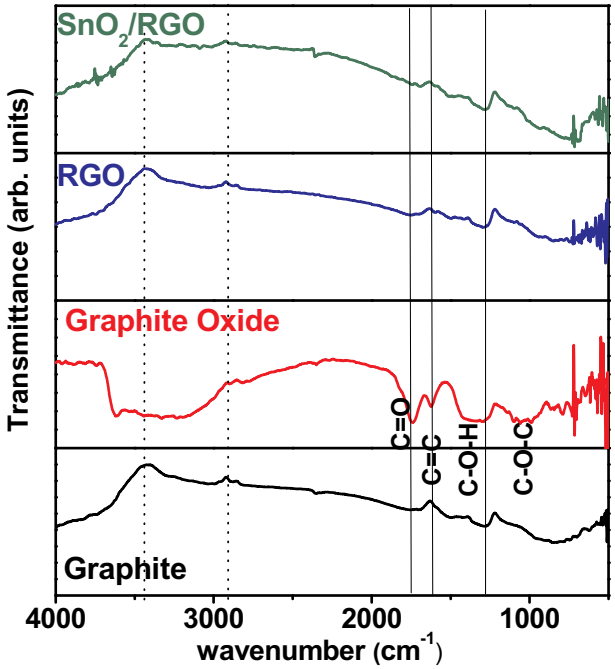

Fig. 5. FTIR spectra of graphite, graphite oxide, RGO, and SnO_2/RGO nanohybrid.

immediately kept on the cold surface at room temperature (25 °C). This sudden quenching helps to arrest the chemical changes occurring on the sensor surface due to interaction with NO_2 molecules. This is later probed using the XPS and Kelvin probe studies.

2.3. Gas sensing measurements

Gas sensing measurements were performed using the indigenously developed table-top static gas sensing unit, Model No. TPD-BARC-16CH [23] as shown in Fig. 1. The unit is equipped with data acquisition and gas sensing test chambers (250 ml) that can accommodate 7 individual sensors. The unit can simultaneously measure/record the resistance of the 16 sensing elements up to 1 GΩ. For sensing measurements, the sensing film was realized on to a glass substrate using screen printing technique (Dr. Blade's method) followed by annealing at 415 °C for 3.5 h. Gold electrodes were deposited on the sensor surface by thermal evaporation technique (base vacuum: 2×10^{-5} Torr). All the sensor films were deposited on to the glass substrate. Gas sensing measurements were performed in the test unit which has provision to mount the sensor substrate onto the alumina platform (containing heater and reader assembly). The sensor response (SR) is calculated from the response curves and using the equation;

$$SR = R_g/R_a \quad (1)$$

where, R_g and R_a are resistances in test gas and ambient air, respectively. The response and recovery times were defined as the time taken by the sensor to reach 90% and 10% of final and initial values upon exposure to NO_2 and ambient air, respectively.

3. Results and discussion

3.1. Structural and morphological characterization

XRD patterns of the graphite, graphite oxide, RGO, and SnO_2/RGO nanohybrids are shown in Fig. 2. For graphite, the intense diffraction peak observed at 2θ = 26.11° corresponds to (002) plane with d-spacing of 3.41 Å. The graphite oxide shows diffraction peak at 11.5° with d-spacing of 7.69 Å which indicates oxidation of graphite to graphite oxide. Further, the broad diffraction peak between 20 and 26° is assigned to the (002) plane of RGO nanosheets with an interlayer spacing of 3.73 Å close to the d-spacing of graphite, suggesting a reduction of graphene oxide. For SnO_2/RGO nanohybrids the most prominent diffraction peaks were indexed to the tetragonal structure of SnO_2. It is noteworthy to mention that the strong intense peak at 26.61° is due to the (110) plane of SnO_2 overlapping with the (002) peak of RGO. The presence of weak diffraction peak at 42.2° assigned to the (100) planes of RGO confirms the formation of SnO_2/RGO nanohybrids. An increase in the annealing temperature leads to a decrease in the full width at half maxima (FWHM, Fig. 2b) that suggests an increase in the crystallite size.

The Raman spectra of graphite (Fig. 3) show the prominent

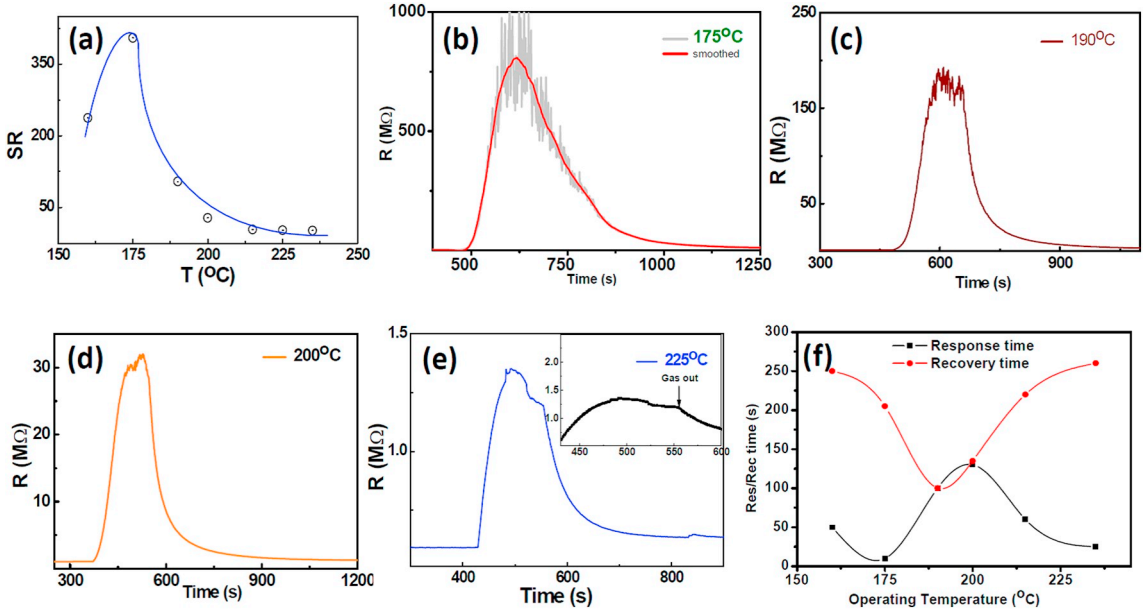

Fig. 6. (a) Effect of operating temperature on sensor response of SnO_2/RGO nanohybrid. Response curves recorded at an operating temperature of (b) 175, (c) 190, (d) 200 and (e) 225 °C with an inset showing the saturation in sensor response upon exposure to NO_2, and (f) variation in response and recovery times with operating temperatures.

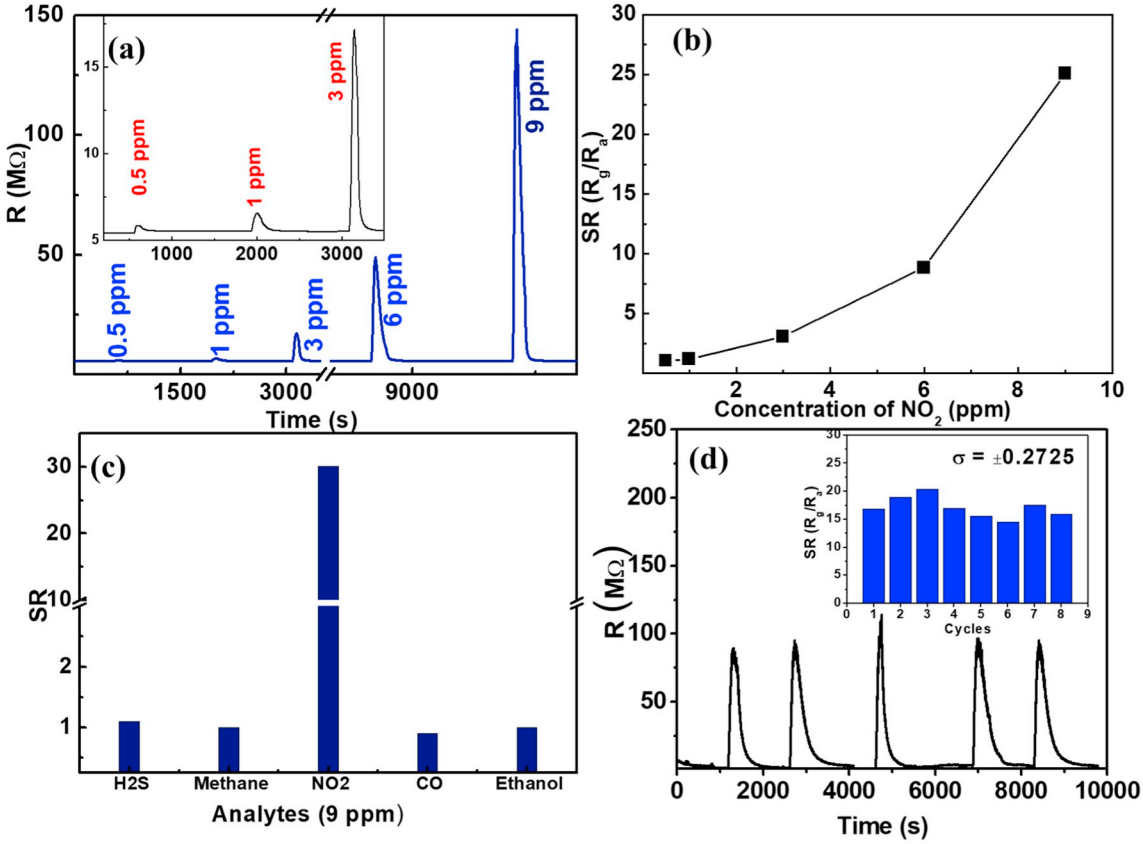

Fig. 7. (a) Response curve recorded as a function of NO_2 concentration with an inset showing the response curves for the low concentrations of 0.5, 1.0 and 3.0 ppm of NO_2 gas, (b) variation of sensor response with gas concentration, (c) selectivity histogram recorded for the 9 ppm of different gases, and (d) repeatability measurement performed by exposing the sensor to 8 ppm of NO_2. The inset shows the standard deviation in the sensor response for 8 consecutive cycles.

graphitic band (G-band) and D-band at 1560 and 1326 cm^{-1}, respectively. In nanohybrids, the G-band shifting towards the higher wavenumber confirms the formation of nanohybrid/nanocomposite and an electronic interaction between $SnO_2$and RGO nanosheets. From the relative intensities of D and G-band, the defect densities have been calculated and are shown in Table 1. It is observed that the graphite has fewer defects as compared to that exhibited by nanohybrids and RGO. However, in nanohybrids, the defect decreases after the post annealing treatment corroborating the XRD findings. Fig. 3c shows the Raman spectra recorded for the nanohybrids prepared using different Sn/GO weight ratio of 13.2, 15.6 and 18.7, respectively. The peaks present around 620 and 560 cm^{-1} are assigned to the A_{1g} vibration mode and the surface phonon mode of SnO_2. The I_D/I_G ratio for these nanohybrids was found to be 1.67, 1.72 and 1.88, respectively. This suggests that the nanohybrids synthesized using Sn/GO ratio of 13.2 have minimum defects. This further implies that the reduction in the structural defects causes reduction in the scattering centres in the RGO. In view of this the composition containing Sn/GO ratio of 13.2 was selected for all the further measurements.

Fig. 4 shows the TEM micrographs of RGO and SnO_2/RGO nanohybrids. The reduction of GO is known to cause a decrease in the number of multilayer's (Fig. 4a). The hexagonal selected area electron diffraction (SAED) pattern in Fig. 4b further indicates crystalline nature of RGO. In nanohybrids, SnO_2 nanoparticles having a size of 5–7 nm are found evenly distributed on the RGO nanosheets (Fig. 4e, f). The combination of ring pattern and hexagonal bright spots in SAED pattern (Fig. 4d) further confirms the formation of nanocomposites/nanohybrids.

Fig. 5 shows the FTIR spectra recorded for graphite, graphite oxide, RGO and SnO_2/RGO nanohybrids. Graphite does not contain any special functional groups on its surface and accordingly, no prominent peaks are seen. The peak at 1698 cm^{-1} is ascribed to the skeletal vibrations of sp^2 hybridized carbon atoms in C═C of honeycomb lattice. The oxidation of graphite, the absorption peaks due to C═O stretching of COOH, C—O stretching, epoxy symmetrical ring C–O–C deformation vibrations, phenolic C–O–H stretching getting incorporated in the graphite can be seen from the peaks appearing at 1742, 1058, 1240 and 1400 cm^{-1} respectively. The broad absorption band at 3160–3635 cm^{-1} is assigned to the -OH stretching vibration arising due to the intercalated moisture content and the strong oxidation. The absorption peak at 1620 cm^{-1} represents the sp^2 character.

3.2. Gas sensing characteristics

Fig. 6 shows the response curves of the sensor film recorded towards 10 ppm of NO_2 at different operating temperatures. A good response curve is evident at an operating temperature of 200 °C for which the sensor response of 29 and response/recovery times of around 130/140 s, respectively were obtained. Although the nanohybrids exhibited a maximum response at 175 °C with SR value of ~400, the noise in the signal was observed to be large. The response and recovery times for different operating temperatures are plotted in Fig. 6f. The improved signal to noise ratio coupled with the faster response kinetics indicates that the 200 °C is more suitable. It is noteworthy to mention that the SnO_2/RGO nanohybrids exhibited a drastic variation in the resistance upon exposure to NO_2. The indigenous test set-up namely the table top static gas sensing unit is able to detect the resistance up to 1 GΩ. For higher values > 1 GΩ there is a significant increase in the noise which is evident in the Fig. 6b–e. This was also the reason to choose 200 °C as the best temperature wherein the resistance change was in the acceptable range of the instrument. An inset of Fig. 6e shows the saturation in the response curve obtained upon exposure to NO_2. Fig. 7 shows the

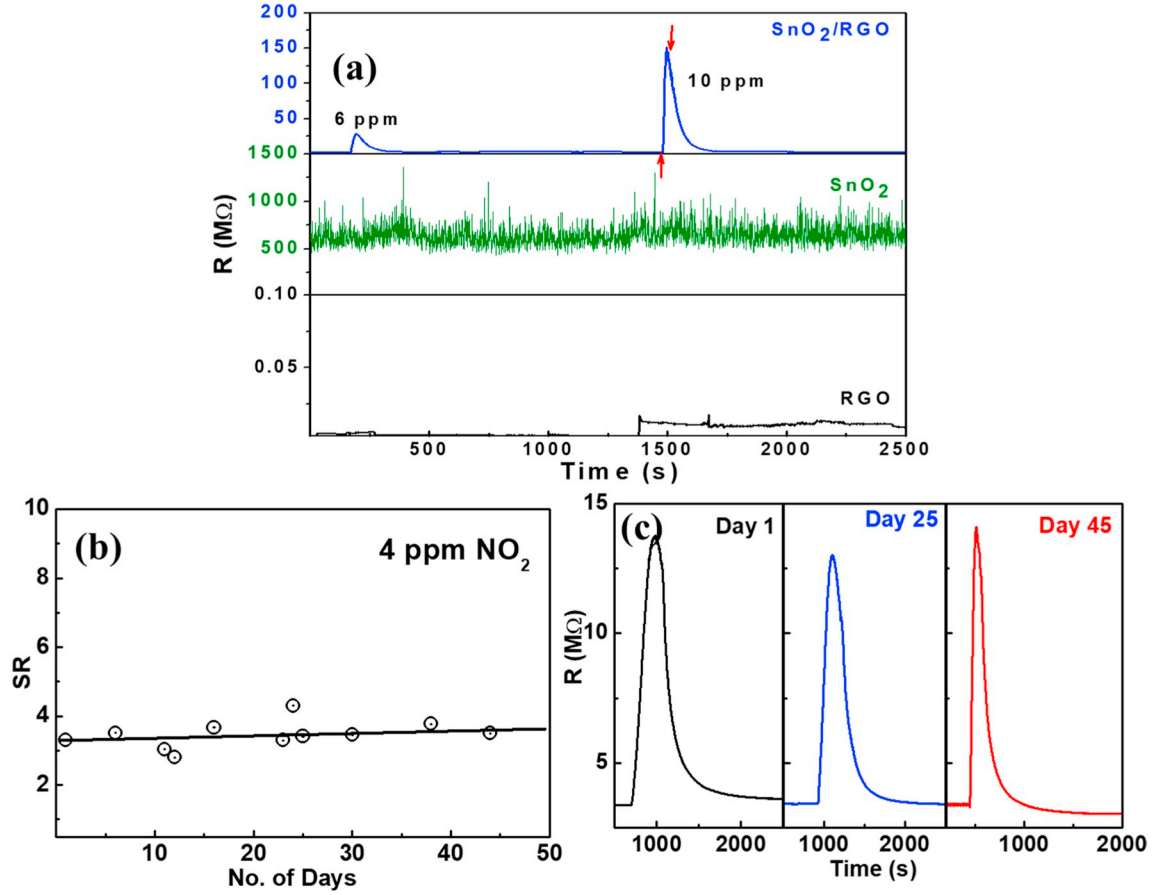

Fig. 8. (a) Comparative response curves recorded for SnO_2/RGO nanohybrids, pure SnO_2 and RGO films upon exposure to 6 and 10 ppm of NO_2 at 200 °C, (b) long term stability performance of the sensor recorded over 45 days period and (c) response curves recorded on 1st, 25th and 45th day upon exposing the sensor film to 4 ppm of NO_2.

Table 2
Comparison of SnO_2/RGO nanohybrid sensor performance with the literature.

Sr. no	Materials	T (°C)	SR	Detection limit	Range (ppm)	Res./rec. time	Ref.
1.	SnO_2/RGO	75	R_a/R_g = 700 (1 ppm)	50 ppb	0.050–2000	11/6 min	[24]
2.	SnO_2/N-RGO	RT	1.38 (5 ppm)	1 ppm	1–5	45/168 s	[25]
3.	rGO-In_2O_3	74	1337 (1 ppm)	10 ppb	0–1000	208/516 s	[26]
4.	NiO-rGO + SnO_2 nanoplates	RT	62.27 (60 ppm)	5 ppm	5–60	220/835 s	[27]
5.	ZnO/RGO	RT	3.5 (5 ppm)	5 ppm	5–50	25/15 s	[28]
6.	ZnO/RGO	300	46.41 (10 ppm)	1 ppm	1–10	99/66 s	[29]
7.	SnO_2	150	556 (40 ppm)	5 ppm	5–100 ppm	100/48 s	[30]
8.	WS_2/WO_3	150	10 (1 ppm)	40 ppb	40 ppb–1 ppm	5/10 min.	[31]
9.	ZnO/MWCNT	300	R_a/R_g = 1.025 (10 ppm)	1 ppm	1–10	93.1/285.2 s	[32]
10.	ZnO/RGO	RT	R_a/R_g = 9.61 (at 50 ppm)	5 ppb	0.005–0.5	4.3/4.8 min	[33]
11.	CVD graphene	RT	S = 1.409 ppm^{-1} (1–25 ppm)	1 ppm	1–25 ppm	Min	[34]
12.	NiO/CuO	RT	R_a/R_g = 4.3 (at 100 ppm)	1 ppm	1–100	2 s	[35]
13.	SnO_2/RGO	200	R_g/R_a = 4.56 (4 ppm)	0.5 ppm	1–9	10/20 s	Present Work

response curves recorded for different NO_2 concentrations. Upon exposure to 3 ppm of NO_2, the sensor exhibited about 3-fold change in resistance. Fig. 7b shows the calibration curve for the sensor recorded over the range from 1 to 9 ppm of NO_2. An exponential increase in sensor response with gas concentration is observed. The selectivity histogram as depicted in Fig. 6c indicates that the sensor shows 30-time

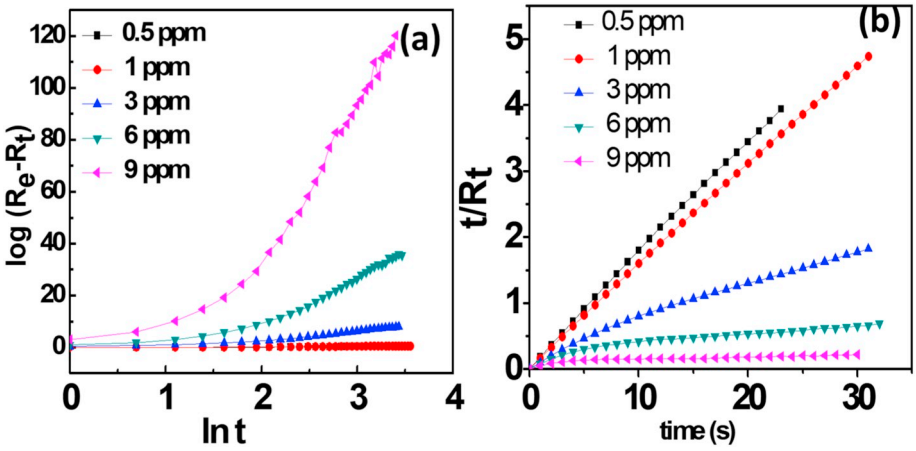

Fig. 9. NO_2 adsorption kinetics on SnO_2/RGO nanohybrids using (a) Elovich model, and (b) Pseudo second order reaction equation.

Table 3
Different metal oxides and their sensor response.

Sr. no.	Materials	Nanostructure size (nm)	Debye length (nm)	Sensor response	LOD (ppm)	Res./rec. time (s)	Ref.
1.	Au NRs/TiO_2 ultra-thin films (H_2) at 250 °C.	15	10	600% (100 ppm)	100	0.6/4	[43]
2.	V: ZnO (acetone) at 300 °C.	< 9	20	95 (100 ppm)	100	46/79	[44]
3.	ZnO NF (NO_2) at 100 °C.	8	20	0.26(25 ppb)	0.025	178/374	[45]
4.	ZnO (NO_2) at 250 °C.	25–35	20	15(0.5 ppm)	2.5	4/242	[46]
5.	SnO_2 NRs (ethanol) at RT.	40	3	0.87 (18 ppm)	3	–	[47]
6.	ZnO NS (NO_2) at 180 °C.	20	20	19(100 ppm)	1	3/12	[48]
7.	SnO_2/graphene	4–6	3	100% (100 ppb)	5 ppb	–	[49]
8.	SnO_2-RGO (NO_2) at 200 °C.	5	3	4 (4 ppm)	0.5	10/100	Present work

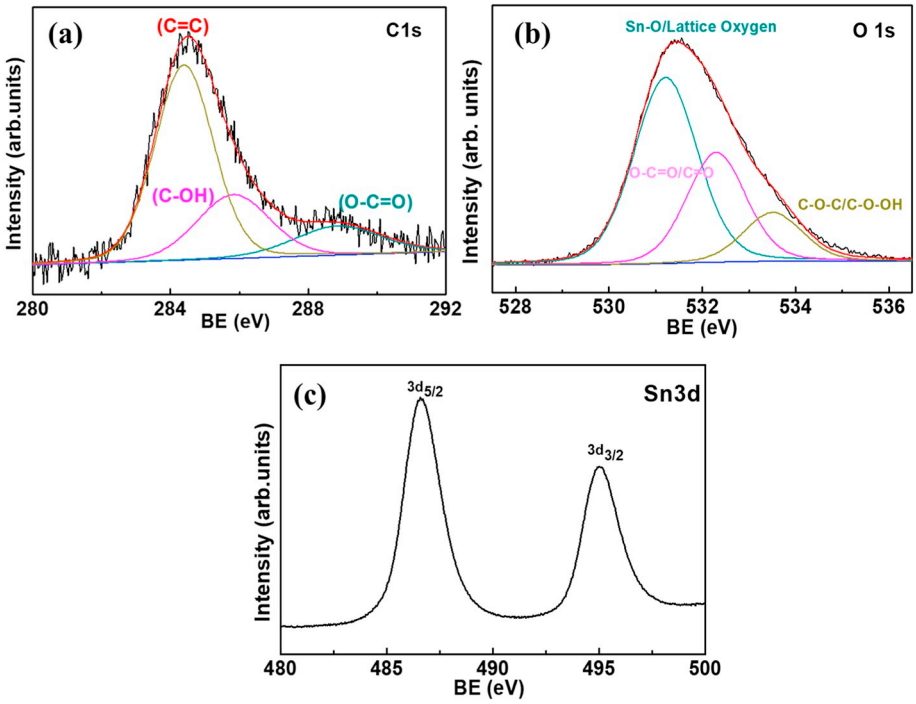

Fig. 10. Deconvoluted spectra of (a) C1s, (b) O1s and (c) Sn 3d peaks of SnO_2/RGO nanohybrids.

better selectivity for NO_2 as compared to that of other analytes. To check the repeatability, the sensor film was subjected to successive NO_2cycles and the obtained response curves are shown in Fig. 7d. A standard deviation of 0.27 in response measured over 8 cycles implies an excellent repeatability of the nanohybrids. For comparison, the response of pure SnO_2 and RGO were also recorded and are shown in Fig. 8. As compare to pristine SnO_2 and RGO, the nanohybrids exhibited enhanced response towards NO_2 implying the importance of the formation of nanohybrids. The long-term stability of the sensor plays a crucial role in its commercial acceptance and deploy-ability. Accordingly, the response of the present sensor was monitored over a period of 45 days as shown in Fig. 8b. The variation in sensor response was found to be < 7% implying good stability of the sensor. For better comparison Fig. 8c shows the response curves recorded at 1st, 25th and 45th day.

Table 4
C1s bond percentage of SnO_2/RGO nanohybrid film.

C 1s	Before NO_2 exposure (at.%)	After NO_2 exposure (at.%)
-C=C	62%	53%
-C-N/-C-OH	25%	37%
O-C=O	13%	10%

Table 5
The atomic percentage of SnO_2/RGO nanohybrid film.

SnO_2/RGO	Before NO_2 exposure (at.%)	After NO_2 exposure (at.%)
C 1s	17%	14%
O 1s	47%	46%
Sn 3d	36%	36%
N 1s	0%	4%

Towards 1 ppm of NO_2, the response and recovery times of SnO_2/RGO nanohybrids were found to be 10 and 20 s, respectively. This faster response kinetics is more effective over some of the reported ones as depicted in Table 2 [24–35].

Although there are number of SnO_2/RGO based gas sensors reported in the literature, but, the effective sensor response, detection limit below TLV and long-term stability makes the present nanohybrids more effective, advantageous and acceptable for the commercial applications. For sensors those are reported to be working at room temperature, the slow response/recovery and chemical instability makes them unsuitable for commercial deployment. Contrary, the present sensor shows good response kinetics, excellent long-term stability and negligible degradation in sensor response over a period of 45 days.

The NO_2 response kinetics of the nanohybrids was further investigated using the Elovich model. This model applies to the chemisorption of the gas molecules on the sensor surface [36,37]. It states that the adsorption probability of gas molecules on the sensor surface decreases exponentially with a number of molecules already adsorbed on the adsorbing surface. It is mathematically represented as;

$$\theta = \frac{1}{\beta}\ln(\alpha\beta) + \frac{1}{\beta}\ln(t) \tag{2}$$

where, θ is the sorption capacity at time t, α is the initial adsorption rate, β is the desorption constant [38]. As, ΔR is the change in resistance with time t which is the result of sorption capacity of NO_2 on the surface of SnO_2/RGO nanohybrid, the applicability of Elovich model can be studied by plotting the values of ΔR vs. ln (t) for different concentration of NO_2. The present experimental data i.e., during the adsorption of gas molecules (during response) for different concentrations of NO_2 (Fig. 9) was studied. The validity of Elovich model is confirmed using the linear fit. It is observed from the Fig. 9a, that at lower concentrations the response kinetics of NO_2 follows the Elovich model. As the concentration of NO_2 increased to 6 and 9 ppm, the linearity starts to decrease. NO_2 response data is further studied using the pseudo second order reaction equation given as,

$$\frac{t}{R_t} = \frac{1}{kR_e^2} + \frac{t}{R_e} \tag{3}$$

where, R_t is the resistance at time t, k is the reaction rate constant ($\Omega^{-1}\,s^{-1}$) and R_e is the equilibrium resistance after exposure of NO_2 [39]. The best linear fit for all the concentration is plotted in Fig. 9b. The linear fit (R^2:0.9992–0.7732) for all the concentrations indicates that the NO_2 adsorption follows the second order reaction kinetics. It also supports the Elovich model which is also of second order. The similar trend of Elovich model is also observed for 6 and 9 ppm where linearity is found to be slightly decreased.

3.3. Sensing mechanism

As observed from TEM, the particle size of SnO_2 is ~5–7 nm which is comparable to twice of its Debye length (3 nm) and accordingly

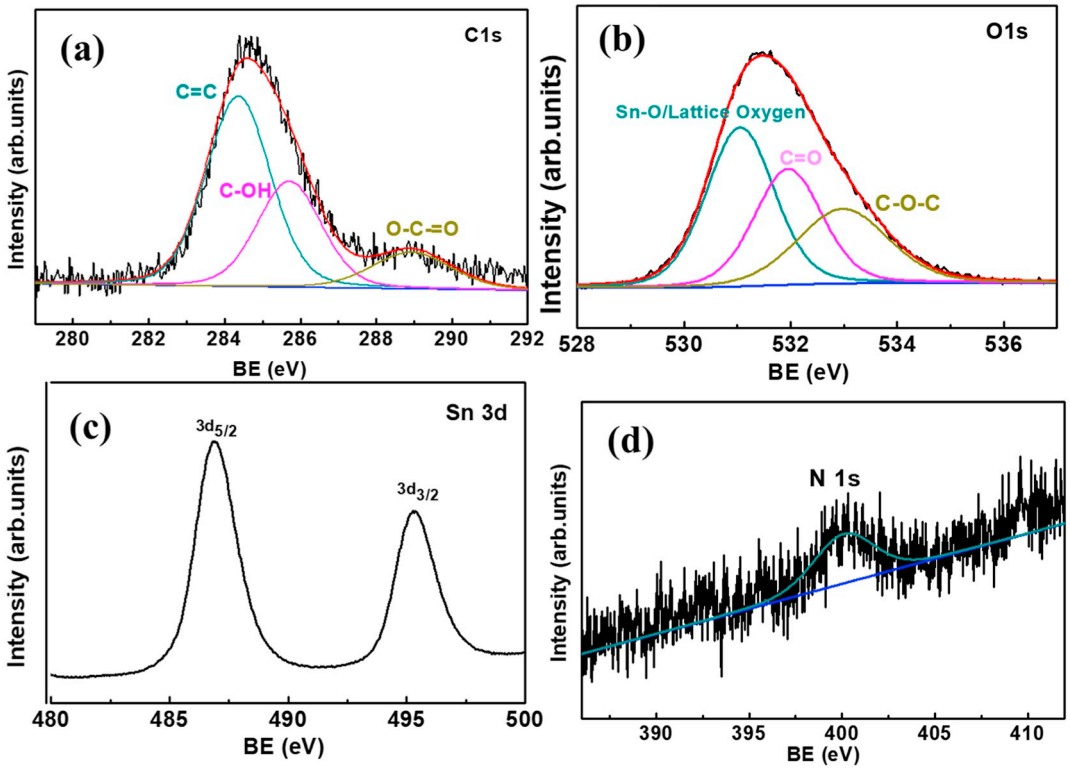

Fig. 11. Deconvoluted spectra for (a) C1s, (b) O1s, (c) Sn 3d, and (d) N 1s of SnO_2/RGO nanohybrids after NO_2 exposure.

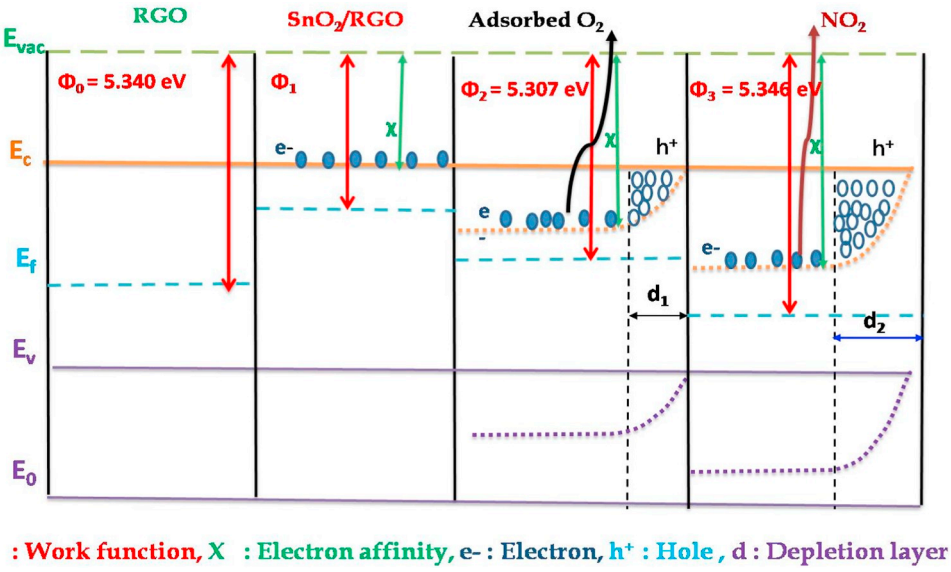

Fig. 12. Schematic representation of the NO_2 sensing mechanism.

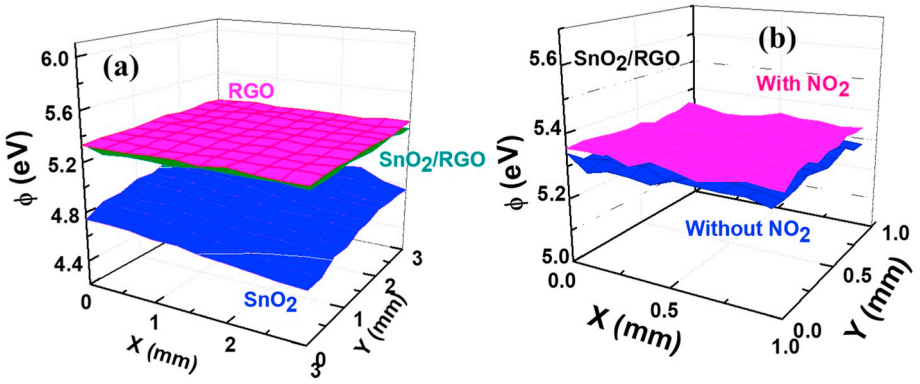

Fig. 13. (a) Work function area map for SnO_2/RGO nanohybrid, SnO_2 and RGO films, and (b) Variation in work function of SnO_2/RGO nanohybrid upon exposure to NO_2 gas.

Table 6
Work function values of pristine and SnO_2/RGO nanohybrid.

Sample	Before NO_2 exposure	After NO_2 exposure
SnO_2	4.945	4.946
SnO_2/RGO	5.306	5.345
RGO	5.340	5.354

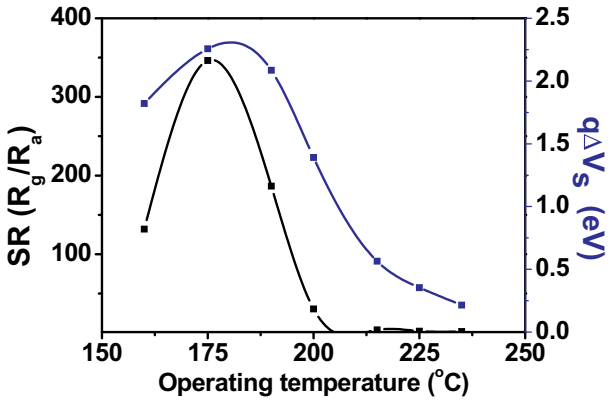

Fig. 14. Operating temperature versus change in surface band bending ($q\Delta V_s$) of SnO_2/RGO nanohybrid upon exposure to 10 ppm of NO_2.

benefits the charge transport and the sensor response [40]. As per semi-quantitative model the sensor response of the material increases when the size of the material reduces to nano-dimensions and approaches its Debye length [41,42]. An increase in the sensor response is mainly ascribed to the high surface area to volume ratio coupled with the charge screening effect on the sensor surfaces. In particular, the charge transport across the nanograin results in fully depleted or accumulated grains. Hence for any minor change on the surface charges causes a drastic variation in the sensor conductivity. This mechanism is commonly referred to as a "grain-control mechanism". Table 3 lists the different nanoforms of ZnO, TiO_2 and SnO_2, wherein the enhanced response towards target gases was observed when the size was comparable to their Debye lengths. This further supports the present hypothesis.

To elucidate the underlying mechanism, XPS measurements were performed before and after NO_2 exposure. Fig. 10 shows the XPS spectra recorded for SnO_2-RGO nanohybrids. The C 1s spectrum is deconvoluted into three peaks with binding energies (BE) values of 284.4, 285.8 and 288.8 eV corresponding to C=C, C-OH/C-N and O-C=O functional groups, respectively. The O 1s peaks were also deconvoluted into three peaks at BE values of 531.8, 532.5 and 533.8 eV corresponding to lattice oxygen, C=O and C-O-OH, respectively. The Sn 3d spectrum shows two peaks at 495 and 486.5 eV attributed to the Sn $3d_{5/2}$ and $3d_{3/2}$, respectively. These peaks correspond to the characteristic peaks of the bulk SnO_2 with a peak separation of 8.5 eV. As the BE for

C—N bond overlaps with the C-OH bond, the chemical interaction of N with carbon can be studied by considering the increased percentage of C-OH bond upon exposure to NO_2. As shown in Table 4 and Fig. 11, the percentage of C-N/C-OH ratio increases after NO_2 exposure. Interestingly, NO_2 exposure also causes an appearance of N 1s peak at 400.1 eV having 10% atomic compositions as shown in Fig. 11d. The O1s spectrum also shows three peaks at BE values of 531.2, 532.3 and 533.5 eV attributed to Sn-O/Lattice oxygen, O-C = O/C-O and C-O-C/C-O-OH, respectively. The elemental composition for the present C, O and N is given in Table 5.

SnO_2 is n-type and while RGO is p-type, hence in nanohybrids distribution of SnO_2 in the RGO matrix results in the randomly distributed heterojunctions and the resistance modulation at the interfaces [50]. In p–n heterojunctions, a potential barrier exists at the interface between RGO and SnO_2 and is depicted schematically in Fig. 12. Herein the main role of SnO_2 is as a receptor, anchoring the analytes on its surface, while that of RGO nanosheets is to provide the excellent electronic conduction pathway. Gas sensing is a surface phenomenon and during sensing the contribution of resistance change predominantly occurs at the surface depth of 5–10 nm. Owing to the surface interactions the work function changes are induced in the sensing layer and can easily be measured using Kelvin probe technique. Fig. 13 shows the work function area map recorded for SnO_2, RGO and SnO_2/RGO nanohybrids. The average work function values for all the samples have been tabulated in Table 6. As also evident from Fig. 13 and Table 6, the work function value for nanohybrids lies close to that of RGO. And upon exposure to NO_2, the work function of nanohybrids changes by ~39 meV. A relatively smaller change of 1 and 14 meV is obtained for pure SnO_2 and RGO, respectively. This corroborates the observation of higher sensor response for nanohybrid films.

The work function of the material is known to have two components associated with it, and are given as;

$$\phi = qVs + \chi \quad (4)$$

Here, qV_s is the surface band bending and χ is the electron affinity [51,52]. The change in work function causes the corresponding variation in both surface band bending and electron affinity and is represented as;

$$\Delta\phi = \pm q\Delta V_s \pm \Delta\chi \quad (5)$$

Herein, the electron affinity is known to be a measure of surface dipole moment [53,54]. For n-type SnO_2, the surface band bending i.e., the heterojunction barrier can easily be calculated from the resistance change arising upon exposure to test gas using;

$$q\Delta V_s = kT\ \ln(R_g/R_a) \quad (6)$$

While for p-type RGO it can be calculated using;

$$q\Delta V_s = -2kT\ \ln(R_g/R_a) \quad (7)$$

where, R_a and R_g are the resistances of the sensor film before and after NO_2 exposure, q is the electronic charge, k is the Boltzmann constant and T is the absolute temperature.

The surface band bending for pure SnO_2 and the SnO_2/RGO nanohybrids was calculated using Eq. (6) and found to be 70 and 1392 meV, respectively. While for RGO as no significant variation in resistance was observed upon NO_2 exposure, the changes in the surface band bending could not be determined. Putting these values in Eq. (5) the change in electron affinity ($\Delta\chi$) for pristine SnO_2 and SnO_2/RGO is found to be around −69 and −1341 meV, respectively. Here, the negative signs imply the decrease in electron affinity after NO_2 exposure and attributed mainly to the negative surface dipole arising due to the interaction between NO_2 and sensor surface [55]. The Kelvin probe measurements and the simplified form of Eq. (4) were also used to calculate the surface band bending at different operating temperatures that significantly alters the sensor surface. Accordingly, Fig. 14 shows the trend observed in sensor response and $q\Delta V_s$ with operating temperature, wherein the maximum is observed at an operating temperature of 175 °C. This implies that the formation of the potential barrier at the interface between RGO and SnO_2 and its variation with NO_2 exposure predominantly alters/improves the sensor response.

4. Conclusion

In conclusion, the SnO_2/RGO nanohybrids exhibiting excellent NO_2 sensing characteristic has been successfully synthesized using the hydrothermal route. The nanohybrids are able to detect NO_2below its threshold limit with a minimum detection limit of 0.5 ppm. The response towards NO_2 obeys the second order reaction kinetics as per the Elovich model. A plausible sensing mechanism is proposed based on the sensing characteristics, Kelvin probe and XPS results before and after exposure to NO_2. The enhanced sensor response coupled with the excellent sensing characteristics namely faster response kinetics and long-term stability demonstrates nanohybrids as an excellent NO_2 sensor. Our results clearly indicate that the SnO_2/RGO nanohybrids can be looked upon as a potential candidate for NO_2 sensing application.

Acknowledgements

One of the authors, BKB acknowledges BARC-SPPU collaborative program for financial support (GOI-E-177). Authors also thank Japan Science Technology Agency (JST) for the support under the SAKURA exchange program in science.

References

[1] M.J. Bechle, D.B. Millet, J.D. Marshall, Does urban form affect urban NO_2? Satellite based evidence for more than 1200 cities, Environ. Sci. Technol. 51 (2017) 12707–12716.
[2] S.K. Sahu, S.H. Kota, Significance of PM2.5 air quality at Indian capital, Aerosol Air Qual. Res. 17 (2017) 588–597.
[3] Z. Zhang, M. haq, Z. Wen, Z. Ye, L. Zhu, Ultrasensitive ppb-level NO_2 gas sensor based on WO_3 hollow nanospheres doped with Fe, Appl. Surf. Sci. 434 (2018) 891–897.
[4] Y. Tian, X. Zhang, H. Shen, A. Liu, Z. Zhao, M.-L. Chen, X.-W. Chen, High time-resolution optical sensor for monitoring atmospheric nitrogen dioxide, Anal. Chem. 89 (2017) 13064–13068.
[5] J.-B. Chen, B. Li, Y. Xiong, J. Sun, A novel turn-off fluorescent probe based on TICT for the detection of NO_2 and nitramines with high sensitivity and selectivity, Sensors Actuators B Chem. 255 (2018) 275–282.
[6] A. Gholizadeh, D. Voiry, C. Weisel, A. Gow, R. Laumbach, H. Kipen, M. Chhowalla, M. Javanmard, Toward point-of-care management of chronic respiratory conditions: electrochemical sensing of nitrite content in exhaled breath condensate using reduced graphene oxide, Microsys. Nanoeng. 3 (2017) 17022.
[7] L. Li, S. He, M. Liu, C. Zhang, W. Chen, Three-dimensional mesoporous graphene aerogel-supported SnO_2 nanocrystals for high-performance NO_2 gas sensing at low temperature, Anal. Chem. 87 (2015) 1638–1645.
[8] A.A. Mane, M.P. Suryawanshi, J.H. Kim, A.V. Moholkar, Fast response of sprayed vanadium pentoxide (V_2O_5) nanorods towards nitrogen dioxide (NO_2) gas detection, Appl. Surf. Sci. 403 (2017) 540–550.
[9] S.S. Shendage, V.L. Patil, S.A. Vanalakar, S.P. Patil, N.S. Harale, J.L. Bhosale, J.H. Kim, P.S. Patil, Sensitive and selective NO_2 gas sensor based on WO_3 nanoplates, Sensors Actuators B Chem. 240 (2017) 426–433.
[10] T. Hojati, M. Ebrahimi, R. Afzalzadeh, Highly sensitive CO sensor based on ZnO/MWCNT nano sheet network grown via hydrothermal method, Mater. Chem. Phys. 207 (2018) 50–57.
[11] A. Kumar, P. Jha, A. Singh, A.K. Chauhan, S.K. Gupta, D.K. Aswal, K.P. Muthe, S.C. Gadkari, Modelling of gate bias controlled NO_2 response of the PCDTBT based organic field effect transistor, Chem. Phys. Lett. 698 (2018) 7–10.
[12] Z. Yuan, J. Zhang, F. Meng, Y. Li, R. Li, Y. Chang, J. Zhao, E. Han, S. Wang, Highly sensitive ammonia sensors based on Ag-decorated WO_3 nanorods, IEEE T. Nanotech. 17 (2018) 1252.
[13] F. Meng, H. Zheng, Y. Sun, M. Li, J. Liu, Triethylamine sensor based on Au modified hierarchical porous single crystalline ZnO nanosheets, Sensors 17 (2017) 1478.
[14] F. Meng, H. Zheng, Y. Chang, Y. Zhao, M. Li, C. Wang, Y. Sun, J. Liu, One-step synthesis of Au/SnO_2/RGO nanocomposites and their VOC sensing properties, IEEE T. Nanotech. 17 (2018) 212.
[15] S. Ge, H. Zheng, Y. Sun, Z. Jin, J. Shan, C. Wang, H. Wu, M. Li, F. Meng, Ag/SnO_2/grapheme ternary nanocomposites and their sensing properties to volatile organic compounds, J. Alloys Compd. 659 (2016) 127–131.
[16] Y. Yuan, Y. Wang, M. Wang, J. Liu, C. Pei, B. Liu, H. Zhao, S. Liu, H. Yang, Effect of unsaturated Sn atoms on gas-sensing property in hydrogenated SnO_2 nanocrystals and sensing mechanism, Sci. Rep. 7 (2017) 1231.
[17] N.S. Ramgir, N. Datta, S. Kumar, S. Kailasaganapathi, U.V. Patil, N. Karmakar,

M. Kaur, A.K. Debnath, D.C. Kothari, D.K. Aswal, S.K. Gupta, Effect of Fe modification on H_2S sensing properties of rheotaxially grown and thermally oxidized SnO_2 thin films, Mater. Chem. Phys. 156 (2015) 227–237.
[18] P.-G. Su, L.-Y. Yang, NH_3 gas sensor based on Pd/SnO_2/RGO ternary composite operated at room-temperature, Sensors Actuators B Chem. 223 (2016) 202–208.
[19] J.-H. Kim, A. Katoch, H.W. Kim, S.S. Kim, Realization of ppm-level CO detection with exceptionally high sensitivity using reduced graphene oxide-loaded SnO_2 nanofibers with simultaneous Au functionalization, Chem. Commun. 52 (2016) 3832.
[20] N.S. Ramgir, P.K. Sharma, N. Datta, M. Kaur, A.K. Debnath, D.K. Aswal, S.K. Gupta, Room temperature H_2S sensor based on Au modified ZnO nanowires, Sensors Actuators B Chem. 186 (2013) 718–726.
[21] N.S. Ramgir, C.P. Goyal, P.K. Sharma, U.K. Goutam, S. Bhattacharya, N. Datta, M. Kaur, A.K. Debnath, D.K. Aswal, S.K. Gupta, Selective H_2S sensing characteristics of CuO modified WO_3 thin films, Sensors Actuators B Chem. 188 (2013) 525–532.
[22] N.S. Ramgir, M. Kaur, P.K. Sharma, N. Datta, S. Kailasaganapathi, S. Bhattacharya, A.K. Debnath, D.K. Aswal, S.K. Gupta, Ethanol sensing properties of pure and Au modified ZnO nanowires, Sensors Actuators B Chem. 187 (2013) 313–318.
[23] N.S. Ramgir, R. Datta, K. Avhad, R. Bhusari, M.M. Vedpathak, M. Meera, V.V. Katke, E. Ravisankar, A.K. Debnath, T.K. Saha, K.P. Muthe, S.C. Gadkari, A table top static gas sensing unit: model no. TPD-BARC-16CH, BARC Newsletter (2017) 14–18 May-June.
[24] Y. Xiao, Q. Yang, Z. Wang, R. Zhang, Y. Gao, P. Sun, Y. Sun, G. Lu, Improvement of NO_2 gas sensing performance based on discoid tin oxide modified by reduced graphene oxide, Sensors Actuators B Chem. 227 (2016) 419–426.
[25] Z. Wang, C. Zhao, T. Han, Y. Zhang, S. Liu, T. Fei, G. Lu, T. Zhang, High-performance reduced graphene oxide-based room-temperature NO_2 sensors: a combined surface modification of SnO_2 nanoparticles and nitrogen doping approach, Sensors Actuators B Chem. 242 (2017) 269–279.
[26] J. Liu, S. Li, B. Zhang, Y. Wang, Y. Gao, X. Liang, Y. Wang, G. Lu, Flower-like In_2O_3 modified by reduced graphene oxide sheets serving as a highly sensitive gas sensor for trace NO_2 detection, Coll. Interface Sci. 504 (2017) 206–213.
[27] J. Zhang, J. Wu, X. Wang, D. Zeng, C. Xie, Enhancing room-temperature NO_2 sensing properties via forming heterojunction for NiO-rGO composited with SnO_2 nanoplates, Sensors Actuators B Chem. 243 (2017) 1010–1019.
[28] Z. Liu, L. Yu, F. Guo, S. Liu, L. Qi, M. Shan, X. Fan, Facial development of high-performance room temperature NO_2 gas sensors based on ZnO nanowalls decorated rGO nanosheets, Appl. Surf. Sci. 423 (2017) 721–727.
[29] H.W. Kim, Y.J. Kwon, A.M. Sung, Y.K. Myung, S. Choi, J.H. Bang, S.S. Kim, Synthesis of zinc oxide semiconductors-graphene nanocomposites by microwave irradiation for application to gas sensors, Sensors Actuators B Chem. 249 (2017) 590–601.
[30] D.L. Kamble, N.S. Harale, V.L. Patil, P.S. Patil, L.D. Kadam, Characterization and NO_2 gas sensing properties of spray pyrolyzed SnO_2 thin films, Anal. Appl. Pyrolysis 127 (2017) 38–46.
[31] F. Perrozzi, S.M. Emamjomeh, V. Paolucci, G. Taglieri, C. Cantalini, Thermal stability of WS_2 flakes and gas sensing properties of WS_2/WO_3 composite to H_2, NH_3 and NO_2, Sensors Actuators B Chem. 243 (2017) 812–822.
[32] Y.J. Kwon, A. Mirzaei, S.Y. Kang, M.S. Choi, J.H. Bang, S.S. Kim, H.W. Kim, Synthesis, characterization and gas sensing properties of ZnO-decorated MWCNTs, Appl. Surf. Sci. 413 (2017) 242–252.
[33] J. Liu, S. Li, B. Zhang, Y. Xiao, Y. Gao, Q. Yang, Y. Wang, G. Lu, Ultrasensitive and low detection limit of nitrogen dioxide gas sensor based on flower-like ZnO hierarchical nanostructure modified by reduced graphene oxide, Sensors Actuators B Chem. 249 (2017) 715–724.
[34] Y. Seekaew, D. Phokharatkul, A. Wisitsoraat, C. Wongchoosuk, Highly sensitive and selective room-temperature NO_2 gas sensor based on bilayer transferred chemical vapor deposited graphene, Appl. Surf. Sci. 404 (2017) 357–363.
[35] H. Xu, J. Zhang, A.U. Rehman, L. Gong, K. Kan, L. Li, K. Shi, Synthesis of NiO@CuO nanocomposite as high-performance gas sensing material for NO_2 at room temperature, Appl. Surf. Sci. 412 (2017) 230–237.
[36] A.K. Debnath, S. Samanta, A. Singh, D.K. Aswal, S.K. Gupta, J.V. Yakhmi, Parts-per-billion level chlorine sensors with fast kinetics using ultrathin cobalt phthalocyanine films, Chem. Phys. Lett. 480 (2009) 185–188.
[37] S. Altın, F. Dumludag, C. Oruc, A. Altındal, Influence of humidity on kinetics of xylene adsorption onto ball-type hexanuclear metallophthalocyanine thin film, Microelectron. Eng. 134 (2015) 7–13.
[38] S. Altun, E.B. Orman, Z. Odabaş, A. Altındal, A.R. Özkaya, Gas sensing and electrochemical properties of tetra and octa 2H-chromen-2-one substituted iron(II) phthalocyanines, Dalton Trans. 44 (2015) 4341–4354.
[39] M.A. Shaker, Thermodynamics and kinetics of bivalent cadmium biosorption onto nanoparticles of chitosan-based biopolymers, J. Taiwan Inst. Chem. Eng. 47 (2015) 79–90.
[40] N. Ramgir, N. Datta, M. Kaur, S. Kailasaganapathi, A.K. Debnath, D.K. Aswal, S.K. Gupta, Metal oxide nanowires for chemiresistive gas sensors: issues, challenges and prospects, Coll. Surf. A 439 (2013) 101–116.
[41] C.N. Xu, J. Tamaki, N. Miura, N. Yamazoe, Grain size effects on gas sensitivity of porous SnO_2-based elements, Sensors Actuators B Chem. 3 (1991) 147–155.
[42] A. Rothschild, Y. Komem, The effect of grain size on the sensitivity of nanocrystalline metal-oxide gas sensors, J. Appl. Phys. 95 (2004) 6374–6380.
[43] O. Lupan, V. Postica, N. Ababii, T. Reimer, S. Shree, M. Hoppe, O. Polonskyi, V. Sontea, S. Chemnitz, F. Faupel, R. Adelung, Ultra-thin TiO_2 films by atomic layer deposition and surface functionalization with Au nanodots for sensing applications, Mater. Sci. Semicond. Process. 87 (2018) 44–53.
[44] Z.E. khalidi, E. Comini, B. Hartiti, A. Moumen, H.M.M. Munasinghe Arachchige, S. Fadili, P. Thevenin, A. Kamal, Effect of vanadium doping on ZnO sensing properties synthesized by spray pyrolysis, Mater. Des. 139 (2018) 56–64.
[45] A. Aziz, N. Tiwale, S.A. Hodge, S.J. Attwood, G. Divitini, M.E. Welland, Core–shell electrospun polycrystalline ZnO nanofibers for ultra-sensitive NO_2 gas sensing, ACS Appl. Mater. Interfaces 10 (2018) 43817 − 43823.
[46] C. Thi Quy, N.X. Thai, N.D. Hoa, D.T. Thanh Le, C.M. Hung, N.V. Duy, N.V. Hieu, C_2H_5OH and NO_2 sensing properties of ZnO nanostructures: correlation between crystal size, defect level and sensing performance, RSC Adv. 8 (2018) 5629–5639.
[47] S. Xu, H. Zhao, Y. Xu, R. Xu, Y. Lei, Carrier mobility-dominated gas sensing: a room-temperature gas-sensing mode for SnO_2 nanorod array sensors, ACS Appl. Mater. Interfaces 10 (2018) 13895 − 13902.
[48] C. Xiao, T. Yang, M. Chuai, B. Xiao, M. Zhang, Synthesis of ZnO nanosheet arrays with exposed (100) facets for gas sensing applications, Phys. Chem. Chem. Phys. 18 (2016) 325–330.
[49] F.-L. Meng, H.-H. Li, L.-T. Kong, J.-Y. Liu, Z. Jin, W. Li, Y. Jia, J.-H. Liu, X.-J. Huang, Parts per billion-level detection of benzene using SnO_2/grapheme nanocomposite composed of sub-6 nm SnO_2 nanoparticles, Anal. Chim. Acta 736 (2012) 100–107.
[50] N. Datta, N. Ramgir, S. Kumar, P. Veerender, M. Kaur, S. Kailasaganapathi, A.K. Debnath, S.K. Gupta, Role of various interfaces of CuO/ZnO random nanowire networks in H_2S sensing: an impedance and Kelvin probe analysis, Sensors Actuators B Chem. 202 (2014) 1270–1280.
[51] D. Gu, X. Li, Y. Zhao, J. Wang, Enhanced NO_2 sensing of SnO_2/SnS_2 heterojunction-based sensor, Sensors Actuators B Chem. 244 (2017) 67–76.
[52] T. Sahm, A. Gurlo, N. Barsan, U. Weimar, L. Madler, Fundamental studies on SnO_2 by means of simultaneous work function change and conduction measurements, Thin Solid Films 490 (2005) 43–47.
[53] M. Hubner, C.E. Simion, A. Tomescu-St˘anoiu, S. Pokhrel, N. Barsan, U. Weimar, Influence of humidity on CO sensing with p-type CuO thick film gas sensors, Sensors Actuators B Chem. 153 (2011) 347–353.
[54] A. Reghu, L. Jay LeGore, J.F. Vetelino, R.J. Lad, B.G. Frederick, Distinguishing bulk conduction from band bending transduction mechanisms in chemiresistive metal oxide gas sensors, J. Phys. Chem. C 122 (2018) 10607 − 10620.
[55] W. Chen, M. Dumas, D. Mao, A. Kahn, Work function, electron affinity, and band bending at decapped GaAs (100) surfaces, J. Vacuum Sci. Tech. B 10 (1992) 1886.